International Journal of Solids and Structures 143 (2018) 232–244

Contents lists available at ScienceDirect

International Journal of Solids and Structures

journal homepage: www.elsevier.com/locate/ijsolstr

Mechanisms and criteria for failure in polycrystalline graphene

C.S. DiMarco*, T. Robillos, J. Hone, J.W. Kysar

Department of Mechanical Engineering, Columbia University, New York, NY, United States

ARTICLE INFO

Article history:
Received 11 October 2017
Revised 3 March 2018
Available online 13 March 2018

Keywords:
Cohesive Zone Model
Graphene
Finite Element Method
Chemical Vapor Deposition
Fracture

ABSTRACT

Graphene is a two-dimensional material that consists of a single layer of carbon atoms covalently bonded in a hexagonal lattice that has incredible mechanical, electrical, and thermal properties. Nanoindentation experiments on freely-suspended circular membranes of mechanically exfoliated single crystal graphene have demonstrated it as the strongest material ever characterized. Chemical Vapor Deposition (CVD) techniques have offered an industrially scalable method to synthesize large area continuous polycrystalline graphene films. Subsequent nanoindentation experiments reveal the presence of grain boundaries only slightly diminishes its strength. Herein, we investigate the probability of failure of grain boundaries in graphene through the Finite Element Method (FEM) within the context of the nanoindentation experiment of a two-grain graphene domain with a single straight grain boundary defined at varying distances from the indentation point. We introduce a novel formulation for a Cohesive Zone Model (CZM) within membrane elements to admit fracture within the grain boundary that accounts for the nonplanar kinematics of membranes. We examine the transition in failure mechanisms from one of rupture within the grain boundary to one of structural instability within the grain. Our analysis reveals three distinct failure regions that provide insight into the factors that influence the probability of failure, such as the indenter tip curvature and the grain boundary properties.

1. Introduction

Graphene is a two-dimensional crystalline material consisting of a single layer of covalently bonded carbon atoms arranged in a hexagonal lattice. Single crystal graphene flakes were first isolated via mechanical exfoliation of graphite crystals (Novoselov et al., 2004). Since then, graphene has received significant attention due to its extraordinary electrical, mechanical, and thermal properties. Nanoindentation experiments of free-standing circular membranes demonstrated single crystal graphene to be the strongest material ever characterized. Additionally, graphene's strength approaches its intrinsic strength which implies an extremely low density of defects (Lee et al., 2008).

Mechanical exfoliation produces small flakes of pristine (i.e. free of defects) graphene, but it is an expensive and time-consuming manual method with low yield. Therefore many efforts have focused on the development of industrially scalable methods to synthesize graphene. Chemical Vapor Deposition (CVD) has proven to be a method capable of growing large area continuous sheets (Kim et al., 2009; Li et al., 2009a). However, CVD graphene typically contains defects such as grain boundaries (line defects) as well as atomic vacancies (point defects). The defects inevitably lead to a decrease in mechanical strength. Nevertheless, with proper processing, this reduction in strength of polycrystalline CVD graphene is minor compared to the strength of pristine single crystal graphene (Lee et al., 2013). This observation motivates the development of a more complete understanding of the mechanics of failure of polycrystalline graphene.

Atomistic scale simulations represent an important class of computational methods available to explore the failure of graphene. These include ab initio methods such as Density Functional Theory (DFT) as well as more phenomenological methods such as Molecular Dynamics (MD). Atomic scale simulations have explored crucial factors such as: (1) atomic arrangement (Malola et al., 2010; Liu et al., 2011; Wei et al., 2012; Zhang et al., 2012), symmetry (Yazyev and Louie, 2010; Cao and Yuan, 2012; Zhang et al., 2013; Han et al., 2014), periodicity (Rasool et al., 2014; Zhang et al., 2015b), and degree of misorientation (Grantab et al., 2010; Liu et al., 2012; Wei et al., 2012; Jhon et al., 2012; 2013; Wu and Wei, 2013) across a grain boundary; (2) dependency on temperature and strain-rate (Yi et al., 2013; Zhang et al., 2013; Chen et al., 2015; Becton et al., 2015); (3) development of more realistic grain structures through algorithms and experimental observations (Kotakoski and Meyer, 2012; Sha et al., 2014a; Jung et al., 2015); (4) effect of grain size (Song et al., 2013; Mortazavi and Cuniberti, 2014; Chen et al., 2015; Yang et al., 2015); and, (5) the effect of

* Corresponding author.
E-mail address: csd2117@columbia.edu (C.S. DiMarco).

https://doi.org/10.1016/j.ijsolstr.2018.03.012
0020-7683/

wrinkles and out-of-plane distortions on mechanical response (Liu and Yakobson, 2010; Yazyev and Louie, 2010; Malola et al., 2010; Hao and Fang, 2012; Zhang et al., 2012). The advantage and appeal of atomistic simulations is the very rich description of phenomena at the level of individual atoms. However, atomistic simulations typically are able to treat only a limited number of atoms at very high applied strain rates. Another drawback is that the length scales of the problem often are inconsistent with experiments. For example, the ratio of the indenter tip to the diameter of the graphene film in Sha et al. (2014b) MD simulations is inconsistent with experiments. This leads to much higher strains at the membrane periphery and therefore unrealistic boundary conditions.

In addition to atomistic simulations, there are two main classes of multiscale simulations that probe the mechanical failure of polycrystalline materials such as graphene. The first class performs studies with atomic scale resolution. These simulations typically have the goal of investigating the physics of rupture at the atomistic scale. They have the advantage of being able to investigate how specific atomic configurations within the grain boundary or other defect contribute to the richness of predicted phenomena. However, a disadvantage is that atomistic scale simulations are very computationally intensive and can only be performed for very small domains over very small time periods at extremely high strain rates. Examples of this type of multiscale simulation are Wang and Guo (2013), Larsson and Samadikhah (2011) and Khare et al. (2007).

The second class of multiscale simulations performs studies at the continuum scale with no explicit atomic scale resolution. This requires that atomic scale phenomena, such as grain boundary rupture, be described in a continuum formulation that contains the salient features associated with the failure process. In the context of grain boundaries, the peak stress and the critical atomic separation at failure along with the free energy of the grain boundary must be specified. These quantities typically are related via a traction vs. separation mathematical relationship that captures the general physics of rupture (Rose et al., 1981). The specific form of the traction vs. separation relationship as well as the peak stress, critical atomic separation at failure and the free energy of the grain boundary are typically determined from atomistic scale simulations. This class of multiscale simulations has the advantage of being able to investigate the mechanics of failure of a system with multiple potential failure paths and mechanisms over large domains and relevant time scales and strain rates. Importantly, this makes it possible to address the competition between the activation of various failure mechanisms in a material. The disadvantage of this class of multiscale models is that the atomic scale information is "averaged" into continuum values, so the richness of the atomic scale configurations is no longer accessible to the model. Furthermore, once the atomistic scale information has been expressed in continuum values, the simulation loses the atomic scale resolution.

The only multiscale models that have been developed to date for grain boundary fracture in graphene are applicable for nanocrystalline structures. Alian and Meguid (2017) presented Finite Element Method (FEM) simulations of polycrystalline graphene by meshing the grain boundary with a finite number of elements whose local properties are defined by MD simulations. Additionally, Shekhawat and Ritchie (2016) developed a statistical theory of toughness of polycrystalline graphene based on large-scale MD simulations, but the domains are also restricted to the nanoscale.

Griffith (1921) was the first to examine the energetics of fracture based upon the elasticity solution of a crack of finite length in an infinite plate; the stress field near a crack tip in a linear elastic solid is formally singular. Barenblatt (1959) and Dugdale (1960) introduced the concept of a narrow region along the prolongation of the crack tip that exhibits a nonlinear mechanical response in an attempt to model the fracture process. The result of the analyses was to "smear out" the crack tip into a zone within which the cohesive tractions remain finite. Such a Cohesive Zone Model (CZM) effectively removes the stress singularity from the near crack tip region. The first implementations of a CZM within the context of FEM was by Hillerborg et al. (1976) and Needleman (1987) to model failure in two-dimensional deformation states.

Our specimens are much too large to be simulated with atomistic scale resolution. Therefore, we choose to develop a multiple length scale model that treats the atomic scale phenomena associated with the rupture of grain boundaries as a traction vs. separation relationship. In doing so, we are able to consider the competition between the rupture of grain boundaries and the rupture within the graphene grains. To that end, we develop a CZM that accounts for the kinematics of fracture in a membrane and also incorporates the traction vs. separation relationship determined from previous MD simulations by Guin et al. (2016).

The goal of this paper is to implement a Cohesive Zone Model within a membrane and use it to model the mechanics of failure during nanoindentation of suspended polycrystalline graphene monolayers. In particular, we are interested in the competition between graphene failure in grain boundaries and failure within a grain. We treat graphene as a membrane (i.e. negligible bending stiffness) that can deform arbitrarily both in its local tangent plane and in its out-of-plane direction. The challenge to implement the CZM within the context of a membrane element is that displacements can occur in three dimensions, but the CZM opening tractions are confined to the local tangent plane of the deformed graphene. We employ the CZM to simulate a simplified representation of nanoindentation experiments on free-standing CVD graphene. The graphene specimen is modeled as a free-standing circular membrane with a single straight grain boundary following a chord across the circular domain. The distance of the grain boundary to the indentation point at the center of the membrane is varied to investigate the transition from intergranular failure to intragranular failure. Our results predict the existence of a critical threshold distance between the grain boundary and the indenter tip. Grain boundary fracture occurs if the distance is smaller than the critical distance. Otherwise, the fracture event occurs within the grain just as it occurs in single crystal graphene. Since we are only interested in the incipient failure, dynamic effects are not considered.

This paper is organized as follows. Section 2 presents the background on the experiments and prior modeling results that motivates the development of the CZM and the investigation of the probability of failure in graphene. Section 3 introduces the CZM and presents the kinematic framework to define the tractions and separations across the interface for a cohesive zone embedded in a membrane undergoing arbitrary deformation in the context of the Finite Element Method. Section 4 presents the FEM model and boundary conditions for the nanoindentation of a two-grain graphene domain. Section 5 examines the transition in failure mechanisms and criteria that govern the failure of the FEM simulations. Finally, in Section 6, we summarize and consider the potential subsequent applications of this model in CVD graphene domains that more closely relate to the experimentally observed structures.

2. Experimental motivation and background

The first nanoindentation experiments on single crystal graphene were performed on free-standing circular membranes of mechanically exfoliated graphene from bulk graphite (Lee et al., 2008). The attraction between layers of graphene in

graphite relies on weak Van der Waals forces. These weak forces are exploited to isolate monoatomic layers of graphene via mechanical exfoliation and transfer them onto substrates for testing. The graphene flakes were transferred to a silicon substrate with a silicon dioxide epilayer into which had been etched an array of cylindrical wells of diameter 1 μm and depth 800 nm patterned through standard photolithography techniques. The nanoindenter perpendicularly approached the center of the suspended membrane, identified the surface, and displaced the center of the membrane into the underlying vacant well while measuring the displacement of the indenter tip as well as the reaction force of the graphene onto the indenter tip. The radius of the indenter tip was measured through Transmission Electron Microscopy (TEM) and found to be 16.5 nm. Since the radius of the indenter tip is much smaller than the radius of the suspended membrane, the indenter can be treated as a point load. This assumption allows analysis of the resulting force-deflection response with a semi-empirical cubic relationship to determine the pre-stress and the mechanical stiffness of the membrane. Additionally, the maximum fracture load is extracted simply from the maximum load before failure. A large number of samples were tested to develop a statistical distribution of the pre-stress, stiffness, and fracture load. Full details of the experimental methods and results are described by Lee et al. (2008).

Following the experiments, DFT simulations were performed to calculate the anisotropic nonlinear elastic properties of graphene under arbitrary in-plane tensile deformations (Wei et al., 2009). A unit cell of graphene's lattice was distorted into characteristic deformation states through uniaxial and equibiaxial strain. The results consist of five independent discrete stress-strain responses from an initial unstrained state through material failure. In an effort to connect the DFT results to a continuum description, the existence of a strain energy density potential function was postulated and expanded in a Taylor series to the fifth power in terms of powers of the Lagrangian strain tensor. The 2nd Piola-Kirchhoff stress components were calculated from derivatives of the strain energy density potential function with corresponding work conjugate components of the Lagrangian strain tensor. Upon accounting for crystal symmetries of the graphene lattice, there are fourteen independent nonzero elastic constants. These were determined by least-squares fitting the continuum description to the stress and strain states calculated via DFT. The resulting continuum nonlinear anisotropic elastic constitutive relationship thus represents a multiple length scale model of graphene.

The resulting higher order constitutive relationship was validated (Wei and Kysar, 2012) against the nanoindentation experiments through FEM simulations using the commercially available software ABAQUS/Standard (Hibbitt et al., 2001). The graphene sheet was modeled using bilinear quadrilateral membrane elements and the indenter tip was treated as a rigid frictionless sphere. The constitutive relation was implemented through ABAQUS/Standard using a User Material (UMAT) subroutine. Excellent correspondence was seen when comparing the force-deflection response between the experiments and the simulation. The validation of the 5th-order nonlinear anisotropic elastic constitutive relationship implies that the failure of pristine graphene occurs due to a structural instability in the material and not due to the activation of a defect. This supports the conclusion that single crystal graphene isolated by the mechanical exfoliation of graphite is nearly free of defects and that it achieves its theoretically predicted maximum stress of 33.5 N/m. After normalizing the two-dimensional stress measure by graphene's interatomic spacing in graphite, 0.335 nm, it can be expressed as an effective three-dimensional stress measure. This yields an effective value of 100 GPa for the maximum stress, making single crystal graphene the strongest material ever characterized.

As a result of this immense strength, it is desirable to develop methods of synthesizing large area graphene sheets through an industrially scalable technique. Chemical Vapor Deposition (CVD) has proven to offer one way to produce large area continuous sheets of graphene (Kim et al., 2009; Li et al., 2009a). In CVD, a face-centered-cubic (FCC) metal foil is used as a catalyst inside a tube furnace. In particular, copper foil is primarily used because it produces large-area continuous monolayer graphene due to its low solubility of carbon. The tube furnace is placed under vacuum and heated to just below the melting point of the copper foil. After the copper is annealed for some time with a forming gas, a carbon-based gas mixed with hydrogen is introduced. At this high temperature and due to the catalytic copper substrate, the carbon disassociates and forms numerous nucleation sites on the surface of the copper foil. With sufficient time and conditions, the grains grow radially until they collide and "stitch" together with adjacent grains to cover the entire surface area of the foil. As a consequence of the surface adsorption growth mechanism of graphene on copper (Li et al., 2009b), the crystallographic orientations of the grains are misaligned. Grain boundaries form as the growing grains meet each other; they are one-dimensional defects in the two-dimensional graphene. The grain boundaries have been observed through Dark-Field Transmission Electron Microscopy (DFTEM) (Huang et al., 2011; Lee et al., 2013). The diffraction patterns of an area allows for the crystallographic orientation of each grain to be measured. Additionally, although not directly measured, it is reasonable to expect zero-dimensional defects such as atomic vacancies or substitutional atoms to be introduced during the synthesis. Therefore, graphene synthesized by CVD is polycrystalline. Herein, "CVD" and "polycrystalline" will be used interchangeably to refer to graphene grown by CVD. In particular, "polycrystalline" graphene will be used to distinguish from the "single crystal" graphene produced by mechanical exfoliation.

The density of nucleation sites can be controlled to achieve either large-grain ($\sim$50 μm) or small-grain ($\sim$1 μm) graphene sheets by tuning the growth parameters. The control of the grain size allows for the investigation of the mechanical properties of CVD graphene both with and without the presence of grain boundaries. With respect to the nanoindentation experiments, large-grain CVD graphene yields a much lower probability of activating a grain boundary within a suspended region as opposed to the small-grain CVD graphene where the probability is much higher.

Identical nanoindentation experiments were repeated for both large- and small-grain CVD graphene (Lee et al., 2013). A large number of samples were tested to develop a statistical distribution of the results. Histograms for the stiffness and the fracture load were compared against the results for single crystal graphene. Three important conclusions can be drawn from these results. First, a comparison of the elastic modulus between the three sample sets showed no statistically significant difference. This implies the grains and grain boundaries of polycrystalline graphene together have the same stiffness as single crystal graphene. Second, a comparison of the fracture loads between the single crystal and large-grain polycrystalline graphene also revealed no statistically significant difference, suggesting that any potentially existing zero-dimensional defects within the grains had a sufficiently small density not to affect the mechanical properties. Thus, the mechanical behavior of the grains in polycrystalline graphene are indistinguishable to that of single crystal graphene, so the previously calculated 5th-order nonlinear anisotropic elastic constitutive relation can be utilized in modeling the grains of polycrystalline graphene. Third, a comparison of the fracture loads between the single crystal and small-grain polycrystalline graphene reveals that small-grain graphene has a lower breaking force. Consequently, this diminution in strength can be attributed to the grain boundaries. While there is a compromise in strength, this decrease is relatively small ($\sim$5%)

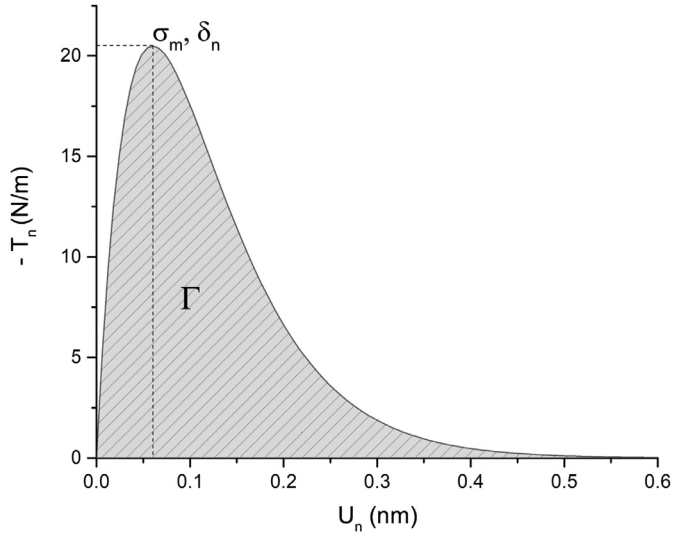

Fig. 1. Traction vs. separation response. T_n from Eq. (3) is plotted with $U_t = 0$ from a point of zero opening to complete decohesion, defined as ten times δ_n.

and still motivates the use of CVD to produce strong graphene films.

3. Membrane-based Cohesive Zone Model

The objective is to develop a CZM to model the rupture of grain boundaries in CVD graphene within an FEM framework. Typically, a CZM is implemented in FEM for two-dimensional deformation states, such as plane stress, plane strain, and axisymmetric deformation. The challenge here is to implement a CZM within a membrane element where displacements can occur in three dimensions but the opening tractions of the CZM are constrained to be within the local tangent plane of the deformed membrane. CZMs are defined by a traction vs. separation relation. Barenblatt (1959) alluded to an expected general form of this relationship which is similar in form to the one seen in Fig. 1. The key feature of this relationship is that the traction reaches a maximum value, σ_m, at some characteristic distance across the interface, δ_n, beyond which is the onset of failure. Needleman proposed a specific functional form of a constitutive relation for an interface for FEM investigations purely for analytical convenience in the form of a polynomial potential function based on maximum tractions and characteristic distances for each degree of freedom involved. By taking derivatives of the potential function with respect to each displacement degree of freedom, the traction vs. separation relationships can be recovered. At minimum, for a traction vs. separation description, the following properties are required for each displacement degree of freedom: (i) a characteristic distance; (ii) a maximum traction; and, (iii) a fracture energy, represented by the area under the traction vs. separation curve. Typically, this information is gleaned from atomistic scale simulations.

3.1. Traction vs. separation relationship

Xu and Needleman (1993) later proposed an exponential form of an interfacial potential function for a two-dimensional deformation state. For analytical convenience, we have chosen to use this form of the potential function in our CZM investigations, which is given by

$$\phi = \phi_n + \phi_n e^{-\frac{U_n}{\delta_n}}\left[\left(1 - r + \frac{U_n}{\delta_n}\right)\left(\frac{1-q}{r-1}\right) - \left(q + \left(\frac{r-q}{r-1}\right)\frac{U_n}{\delta_n}\right)e^{-\left(\frac{U_t}{\delta_t}\right)^2}\right], \tag{1}$$

where $\phi_n = \sigma_m e \delta_n$ is the work of normal separation, σ_m is the maximum stress, δ_n is the characteristic normal distance, δ_t is the characteristic tangential distance, U_n and U_t are the normal and tangential separations, $q = \phi_t/\phi_n$ is the normal-shear coupling where ϕ_t is the work of tangential separation, and $r = U_n^*/\delta_n$ is the normal opening under pure shear where U_n^* is the normal distance after complete separation with zero normal traction.

For the current investigation, we simplify this model by considering zero normal opening under pure shear, $r = 0$, and that the work of tangential separation is equivalent to the work of normal separation, $q = 1$. This yields the simplified potential function

$$\phi|_{r=0,\ q=1} = \phi_n - \phi_n e^{-\frac{U_n}{\delta_n}}\left(1 + \frac{U_n}{\delta_n}\right)e^{-\left(\frac{U_t}{\delta_t}\right)^2}. \tag{2}$$

The interfacial normal, T_n, and tangential, T_t, tractions are determined by taking derivatives of ϕ in Eq. (2) with respect to U_n and U_t, respectively, and yields

$$T_n|_{r=0,\ q=1} = \frac{\partial \phi}{\partial U_n} = -\frac{\phi_n}{\delta_n}e^{-\frac{U_n}{\delta_n}}\left(\frac{U_n}{\delta_n}\right)e^{-\left(\frac{U_t}{\delta_t}\right)^2}$$

$$T_t|_{r=0,\ q=1} = \frac{\partial \phi}{\partial U_t} = -\left(\frac{2\phi_n}{\delta_t}\right)\frac{U_t}{\delta_t}\left(1 + \frac{U_n}{\delta_n}\right)e^{-\frac{U_n}{\delta_n}}e^{-\left(\frac{U_t}{\delta_t}\right)^2}. \tag{3}$$

This relationship is reduced to three independent material parameters. For the current investigation these are defined as $\sigma_m = 20.5 \pm 0.5\,\text{N/m}$, $\delta_n = 0.06 \pm 0.005\,\text{nm}$, and $\delta_t = 0.06 \pm 0.005\,\text{nm}$. Together these three parameters along with the functional form of the traction vs. separation relationship also define the fracture energy, $\Gamma = 2.1 \pm 0.2\,\text{eV/Å}$. These values were defined from MD simulations performed by Guin et al. (2016) on experimentally observed CVD graphene grain boundaries (Huang et al., 2011). Guin et al. (2016) is to date the only researcher to extract traction vs. separation relationships for graphene grain boundaries from atomistic scale simulations of grain boundary rupture. Their results for the peak traction at failure are consistent with other atomistic simulations, as reviewed by Zhang et al. (2015a), which range from 6.7 N/m to 33.5 N/m.

The concept of a cohesive zone implies a high angle grain boundary in which the crystal defects within the grain boundary are so closely spaced that they can be treated with the continuum assumption. However, as discussed by Guin et al. (2016), while high angle grain boundaries can satisfy these conditions, the defect structures in low angle grain boundaries can be spaced so far apart that the continuum approximation of a grain boundary does not hold. Specifically, in our case, we intend to model high angle grain boundaries such that the average distance between crystal defects within the grain boundary is much smaller than the radius of the indenter tip, so that the continuum assumption is valid.

Due to the axisymmetry of the nanoindentation experiment, the suspended CVD graphene membrane is primarily under a state of equibiaxial stress under and near the spherical indenter tip. Accordingly, we expect the failure mode in the grain boundary, and hence the CZM, to be predominantly due to normal traction. Therefore, in Fig. 1, T_n from Eq. (3) is plotted assuming zero tangential separation, $U_t = 0$, to gain insight into failure of the CZM within the context of the nanoindentation experiments.

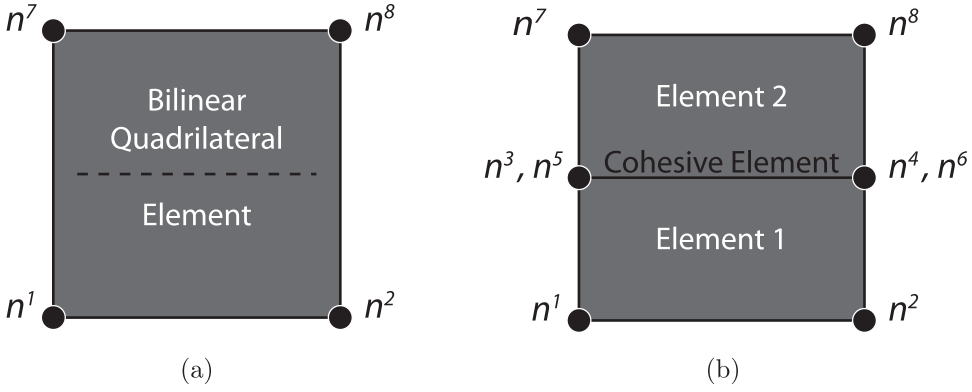

Fig. 2. Insertion of a cohesive zone element within a bilinear quadrilateral element. (a) A single four-node quadrilateral element prior to cohesive element insertion. The dotted line represents a bisector of the element for the insertion of a cohesive zone element. (b) A three-element representation and connectivity of a zero thickness four-node cohesive zone element between two quadrilateral elements.

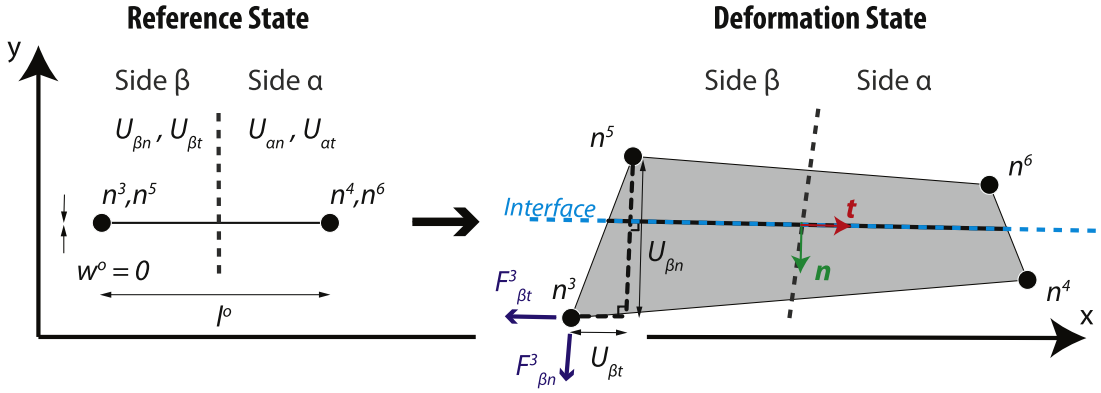

Fig. 3. Kinematics of a two-dimensional four-node cohesive zone element. A schematic of a single element from its unstrained reference state (on the left) to a general deformation state (on the right).

3.2. Two-dimensional CZM kinematics

First, let us examine the implementation of a CZM in a simpler two-dimensional example to gain insight into the formulation of the kinematics. For this discussion, we utilize a subscript to identify the degree of freedom and a superscript to identify the node number for the variables involved. Consider, as shown in Fig. 2a, a single four-node bilinear quadrilateral plane strain element. A cohesive zone element can be realized through a simple bisection of this element and insertion of four interface nodes to define the connectivity of the cohesive zone element. This results in a three-element arrangement with the cohesive zone element encased between two adjacent plane strain elements as shown in Fig. 2b.

The following kinematic formulation follows directly from Becker (1988). A general two-dimensional deformation state of a cohesive zone element has two displacement degrees of freedom across the interface: a normal, U_n, and a tangential, U_t, opening. As shown on the left in Fig. 3, in an unstrained reference state, the cohesive zone element is defined as a one-dimensional line with a finite initial length, l^o, and an initial width (or opening), w^o, of zero. As is shown by the vertical dotted lines in Fig. 3, the cohesive zone interface is divided into two sides, α and β, such that each side spans half the length of the interface. The location of the two nodes on either side are initially coincident, and both U_n and U_t are defined with respect to the nodal positions for each side. As the cohesive zone element stretches into a general two-dimensional deformation state, shown on the right in Fig. 3, a Cartesian local coordinate system (**n**, **t**) is defined with respect to the interface in order to define the normal, **n**, and tangential, **t**, vector directions. In this simple two-dimensional example, the interface, indicated in Fig. 3, can easily be defined by utilizing the vector that connects the midpoint between nodes 3 and 5 and the midpoint between nodes 4 and 6. **t** is defined to be collinear with the interface. Subsequently, **n** is readily defined perpendicular to **t** following the right-hand rule from **n** to **t**. Based on (**n**, **t**) and the nodal positions, the normal and tangential openings are readily determined for both sides of the cohesive zone element: $U_{\alpha n}$ and $U_{\alpha t}$ for side α and $U_{\beta n}$ and $U_{\beta t}$ for side β. These are also expressed at quadrature points by linear interpolation with two-point Gauss quadrature. Subsequently, T_n and T_t across the interface are evaluated through Eq. (3) for both side α and β and then extrapolated onto each of the nodes as forces. As an example, Fig. 3 explicitly displays the separation for side β and the corresponding nodal forces at node 3, denoted as $F^3_{\beta n}$ and $F^3_{\beta t}$.

3.3. Three-dimensional membrane-based CZM kinematics

Since we are modeling a cohesive zone within the context of nanoindentation experiments of polycrystalline graphene, our goal is to allow for a displacement discontinuity analogous to the bilinear quadrilateral element in Fig. 2a, while generalizing the kinematics of the element to be a membrane with three degrees of freedom at each node. The main challenge is that the entire membrane element itself is able to deform to become non-planar. However, we note that the horizontal dashed line representing the incipient displacement discontinuity in Fig. 2a remains straight even after deformation occurs as long as the vertical sides of the element remain linear. Therefore we choose to apply constraints such that the edge deformations across the interface of the three-element representation seen in Fig. 2b are the same as the origi-

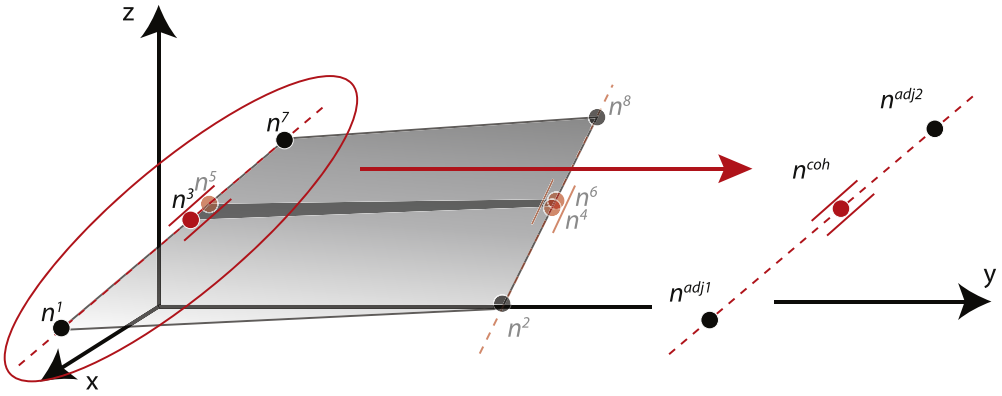

Fig. 4. Multiple Point Constraint of the cohesive zone nodes within the three-element representation in a general three-dimensional deformation state. Two bilinear four-node quadrilateral membrane elements connected by a four-node cohesive zone element. The cohesive zone nodes are represented by nodes 3-6, the lines to which they are constrained are indicated by the dotted lines, and the nodal constraint is represented by the sets of parallel solid lines that border the cohesive element nodes. On the right, this linear MPC is generalized for a single arbitrary cohesive zone node. (For interpretation of the references to color in this figure legend, the reader is referred to the web version of this article.)

nal single-element representation (i.e. nodes 1, 3, 5, and 7 remain collinear and nodes 2, 4, 6, and 8 remain collinear). In other words, the three-element representation is formulated such that the edges across the cohesive zone remain bilinear. Additionally, it is important to note that without a constraint on the cohesive element nodes, the cohesive element is under-constrained. Equivalent to membrane elements, the membrane-based cohesive element can only withstand and transmit in-plane forces. In order to prevent nonphysical sliding of the cohesive zone in the local out-of-plane direction, a kinematic constraint is required. One way membrane structures achieve this is by including a small fictitious damping term which is removed upon reaching a final state to determine the full static solution (Taylor et al., 2005). While this method is not employed within the CZM, it is reasonable to expect it to yield similar results.

We apply this bilinear constraint numerically within ABAQUS/Standard by using a Multiple Point Constraint (MPC) (Hibbitt et al., 2001). It is displayed graphically in Fig. 4 with respect to a general deformation state of the three-element representation. The MPC restricts nodes 3 and 5 each to remain in a straight line between nodes 1 and 7, and restricts nodes 4 and 6 each to remain in a straight line between nodes 2 and 8. While this MPC constraint would consequently limit the potential for a tangential opening across the interface, we do not expect significant tangential opening because (i) membrane elements cannot withstand significant in-plane shear prior to buckling and (ii) the nanoindentation experiment subjects the membrane to an approximately equibiaxial stress state.

In general, as shown on the right side of Fig. 4, the MPC consists of constraining a single cohesive zone node, n^{coh}, on a line defined by two adjacent nodes, n^{adj1} and n^{adj2}. The line defined by the two adjacent nodes will be referred to as the *constraint line*. This three-dimensional linear MPC is a parametric extension of a two-dimensional linear constraint provided as an example by ABAQUS/Standard (Hibbitt et al., 2001). In the example, a MPC restricts a single degree of freedom of a node by eliminating that node's degree of freedom by making it a function of other nodal degrees of freedom involved in the constraint. In two-dimensional space (x, y), a linear MPC is implemented numerically by defining a *constraint equation* based on nodal displacement degrees of freedom, u_i. This is derived by equating the slope defined by n^{coh} and n^{adj1} to the slope defined by n^{adj1} and n^{adj2}, which is given by

$$\frac{x_y^{coh} - x_y^{adj1}}{x_x^{coh} - x_x^{adj1}} = \frac{x_y^{adj2} - x_y^{adj1}}{x_x^{adj2} - x_x^{adj1}}, \tag{4}$$

where x_i are the current nodal coordinates. Note that $x_i = X_i + u_i$, where X_i are the reference nodal coordinates. The plane within which the line is defined will be referred to as the *constraint plane*. The resulting *constraint equation*, f, is given by

$$\begin{aligned} &f(u_x^{coh}, u_y^{coh}, u_x^{adj1}, u_y^{adj1}, u_x^{adj2}, u_y^{adj2}) \\ &\quad = (x_y^{coh} - x_y^{adj1})(x_x^{adj2} - x_x^{adj1}) - (x_y^{adj2} - x_y^{adj1})(x_x^{coh} - x_x^{adj1}) \\ &\quad = 0 \end{aligned} \tag{5}$$

by bringing all of the terms in Eq. (4) to one side so that the expression is equal to zero. Derivatives of Eq. (5) are taken with respect to each nodal u_i to determine the functional relationship of the degree of freedom to be eliminated to the remaining degrees of freedom.

Constraining a node with two degrees of freedom onto a line requires a single degree of freedom to be constrained. In Eq. (5), either the x or the y degree of freedom of n^{coh} could be constrained simply by changing the order in which the derivatives are taken. It is most efficient to constrain the degree of freedom that has the shortest path to satisfying the MPC. This is easily determined by identifying onto which coordinate axis the projection of the *constraint line* is minimized. This is illustrated in Fig. 5a and the notation $C_i(n_{dof}^{coh})$ is introduced to define the constraint used, where the subscript i refers to the *constraint plane*, defined by the outward normal vector, and the function input specifies the constrained nodal degree of freedom. Additionally, the specified *constraint plane* indicates the corresponding *constraint equation*. For example, considering the (x, y) plane, if the projection of the *constraint line* is minimized on the x-axis, then constraining the x degree of freedom of n^{coh} yields the shortest path to satisfying the MPC (i.e. $C_z(n_x^{coh})$); otherwise, the opposite would be true and the y degree of freedom of n^{coh} would be constrained (i.e. $C_z(n_y^{coh})$).

In three-dimensional space (x, y, z), we cannot as readily define the slope of a line with single expression, so a set of parametric equations are necessary. Additionally, to constrain a node with three degrees of freedom onto a line, two degrees of freedom must be constrained. Therefore, we extend the two-dimensional MPC formulation by utilizing a pair of *constraint equations* along with two *constraint planes*. Again, the two degrees of freedom to constrain are identified by determining which two global unit vectors minimize the projection of the *constraint line* vector. Lastly, as illustrated in Fig. 5, there are three possible *constraint planes* to consider. The two *constraint planes* must be carefully chosen because once a degree of freedom is constrained it cannot be used in other calculations for that iteration of the simulation. Clearly, one

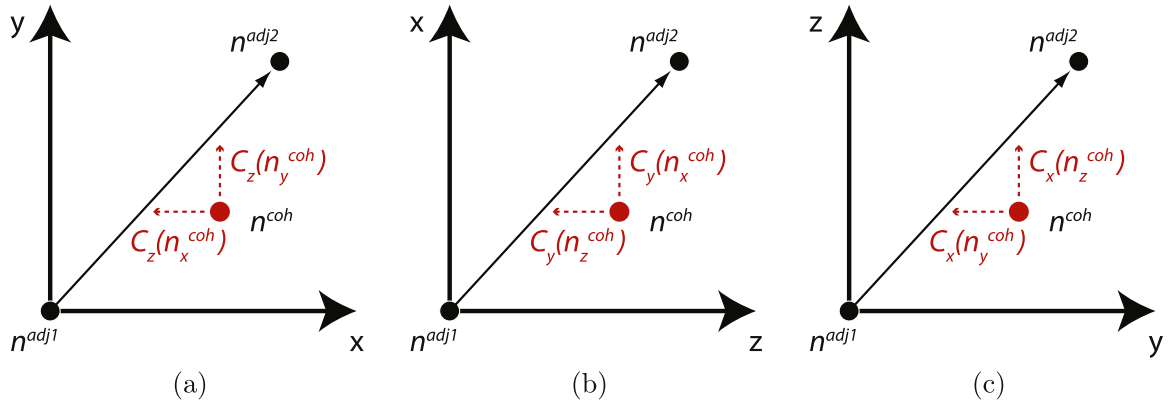

Fig. 5. Three-dimensional linear MPC *constraint planes*, *constraint lines*, and constrained degrees of freedom. These frames illustrate the three *constraint planes* onto which the *constraint line* between n^{adj1} and n^{adj2} is projected: (a) C_z, (b) C_y, and (c) C_x.

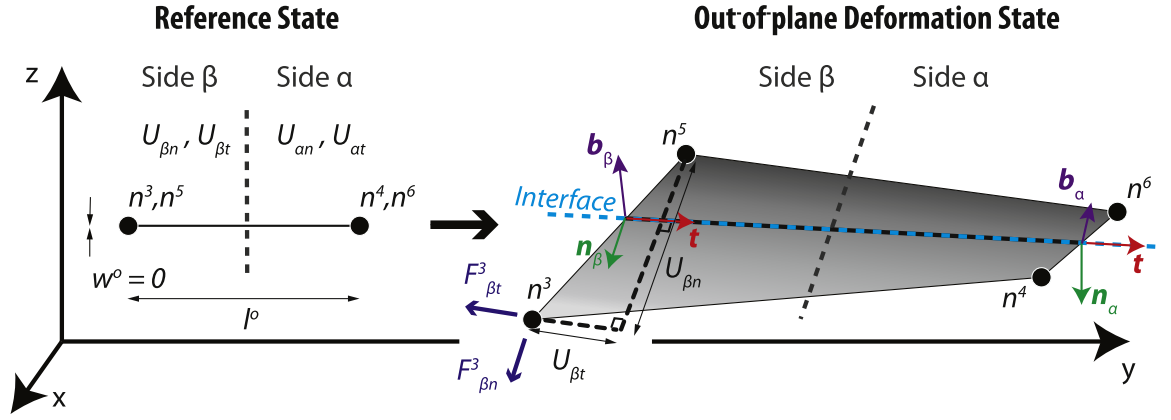

Fig. 6. Kinematics of a three-dimensional four-node membrane-based cohesive zone element. A schematic of the reference state (on the left) of the undeformed four-node cohesive zone element to a general out-of-plane deformation state (on the right).

Cartesian unit vector for each of the two *constraint planes* must correspond with each constrained degree of freedom. Therefore, the second Cartesian unit vector for both *constraint planes* is the same and equivalent to the Cartesian unit vector that maximizes the projection of the *constraint line* vector.

Once the two *constraint planes* and the two constrained degrees of freedom are identified, the two-dimensional *constraint equation* from Eq. (5) can be generalized to

$$\begin{aligned} &f\left(u^{coh}_{dof1}, u^{coh}_{dof2}, u^{adj1}_{dof1}, u^{adj1}_{dof2}, u^{adj2}_{dof1}, u^{adj2}_{dof2}\right) \\ &\quad = \left(x^{coh}_{dof2} - x^{adj1}_{dof2}\right)\left(x^{adj2}_{dof1} - x^{adj1}_{dof1}\right) \\ &\qquad -\left(x^{adj2}_{dof2} - x^{adj1}_{dof2}\right)\left(x^{coh}_{dof1} - x^{adj1}_{dof1}\right) = 0 \end{aligned} \tag{6}$$

and applied for each *constraint plane*, where the nodal degrees of freedom involved and the order of the derivatives are selected accordingly.

Once the kinematics of deformation have been resolved, the primary remaining challenge with implementation is defining U_n and U_t for a membrane-based cohesive zone element. Unlike the two-dimensional case, the four cohesive zone nodes do not remain coplanar for an arbitrary strained state. We must account for both stretching, as well as twisting, in defining U_n and U_t across the interface. As can be seen on the left in Fig. 6, the undeformed reference state of the cohesive zone element within a membrane element is identical to the two-dimensional example from Fig. 3. Once again, the interface is divided into two sides, α and β, and separations are to be defined for each side of the element. For a general out-of-plane deformation state of the cohesive zone element, on the right in Fig. 6, it is immediately apparent that at least two Cartesian local coordinate systems are required, one for each side of the element, to account for the twisting of the element along the interface axis. As shown in Fig. 6, ($\mathbf{n}_\alpha$, $\mathbf{t}$, $\mathbf{b}_\alpha$) is defined for side α and ($\mathbf{n}_\beta$, $\mathbf{t}$, $\mathbf{b}_\beta$) is defined for side β. Synonymous to the two-dimensional example, the unit tangential vector, $\mathbf{t}$, is collinear with interface and is shared between both local coordinate systems. The unit outward normal vector for side α, $\mathbf{b}_\alpha$, is defined by the normalized cross product between $\mathbf{v}^{6,4}$ (the vector from nodes 6–4) and $\mathbf{t}$. Similarly, the unit outward normal vector for side β, $\mathbf{b}_\beta$, is defined by the normalized cross product between $\mathbf{v}^{5,3}$ (the vector from nodes 5–3) and $\mathbf{t}$. The calculations for $\mathbf{b}_\alpha$ and $\mathbf{b}_\beta$ are given by

$$\mathbf{b}_\alpha = \frac{\mathbf{v}^{6,4} \times \mathbf{t}}{\|\mathbf{v}^{6,4} \times \mathbf{t}\|} \qquad \mathbf{b}_\beta = \frac{\mathbf{v}^{5,3} \times \mathbf{t}}{\|\mathbf{v}^{5,3} \times \mathbf{t}\|}. \tag{7}$$

Lastly, the unit normal vectors for each side, $\mathbf{n}_\alpha$ and $\mathbf{n}_\beta$, are defined as the normalized cross product between $\mathbf{t}$ and the corresponding unit outward normal vector, $\mathbf{b}_\alpha$ and $\mathbf{b}_\beta$, and are given by

$$\mathbf{n}_\alpha = \mathbf{t} \times \mathbf{b}_\alpha \qquad \mathbf{n}_\beta = \mathbf{t} \times \mathbf{b}_\beta \tag{8}$$

$U_{\alpha n}$, $U_{\alpha t}$, $U_{\beta n}$, and $U_{\beta t}$, are determined from the nodal displacement vectors for each side with respect to the corresponding local coordinate system. Subsequently, the tractions and nodal forces are determined in the same manner as the two-dimensional example.

There still persists a complication. The planes within which the interfacial tractions are determined, defined by $\mathbf{b}_\alpha$ and $\mathbf{b}_\beta$, do not coincide with the local tangent plane at each cohesive zone node on the corresponding side. This is a result of twisting of the element. The forces must remain in-plane when being transmitted to

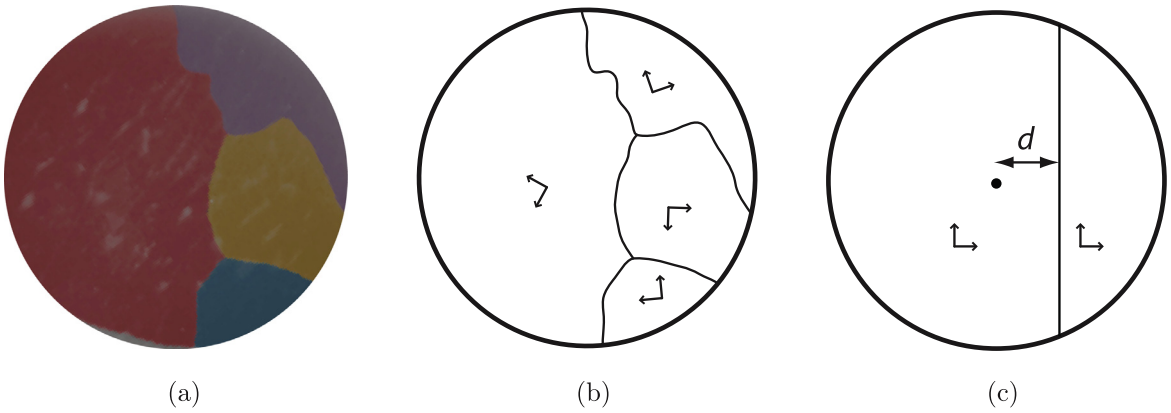

Fig. 7. Simplification of the domain of a suspended polycrystalline graphene membrane. (a) A false-colored DFTEM image of an experimentally observed membrane. Each color corresponds to a graphene grain of which the relative orientation is measured from observing the diffraction pattern. (b) The exact representation of (a) in an FEM domain. (c) A simplified representation with a single straight grain boundary and aligned orientations. (For interpretation of the references to color in this figure legend, the reader is referred to the web version of this article.)

the adjacent membrane elements across the cohesive zone. Thus, the calculated nodal tractions are projected onto the local tangent plane for each node. As long as sufficiently small elements are chosen along the grain boundary, the elemental twist will be minimal and the error introduced from this projection will be negligible.

4. Finite Element Method simulations

We implement the membrane-based Cohesive Zone Model in an FEM simulation of the nanoindentation of freely-suspended circular membranes of polycrystalline graphene using ABAQUS/Standard (Hibbitt et al., 2001). First, we consider the complexities involved with the experiment based on observations of suspended membranes (Lee et al., 2013). One such suspended membrane imaged with DFTEM is seen in Fig 7a. DFTEM and diffraction patterns of suspended membranes reveal that the grain boundaries are not straight and can even be jagged depending on the grain growth morphology and relative orientation to adjacent grains. Depending on the average grain size of the CVD graphene growth, a suspended circular membrane of a given diameter will have a correlated number of grains (and grain boundaries) in its domain. This change in density of grain boundaries will affect the probability of the indenter tip to encounter and activate failure along a grain boundary and will, therefore, influence the probability of failure.

Huang et al. (2011) performed atomic scale imaging of CVD graphene grain boundaries through High-Resolution TEM (HRTEM) that revealed three additional important details: (i) significant non-linearity of grain boundary paths, (ii) adjacent grains typically have asymmetric tilt in crystallographic orientation, and (iii) the atomic configuration of the grain boundaries is atomically complex, composed of non-periodic sequences of primarily pentagonal, hexagonal, and heptagonal rings. In Fig. 7, we show how the domain is simplified for these initial investigations from its exact experimentally observed grain structure in Fig. 7a to a circle with a chord to represent a two-grain membrane and a single grain boundary, respectively, in Fig. 7c.

The simplified domain shown in Fig. 7c is used as a model that contains the minimum salient features necessary to study the failure mechanisms of graphene. A perspective view of the FEM model is shown in Fig. 8b. The diameter of the membrane is $\phi_{mem} = 1\,\mu m$ to match the experiments. The distance, d, is defined as the perpendicular length from the chord to the center of the circular domain. We assume there will be some critical threshold distance, d_c, for which failure will occur within the grain boundary (i.e. $d < d_c$), whereas failure will occur within the grain for $d > d_c$. As a result, the domain has two grains and for simplicity we specify the crystallographic orientation of each grain to be the same for these initial simulations. The crystallographic orientation of graphene is commonly defined by two unit vectors that are aligned with the zigzag and the armchair directions within the lattices. The zigzag and armchair directions can be expressed, respectively, with the Miller-Bravais notation as $[11\bar{2}0]$ and $[1\bar{1}00]$, as seen in Fig. 8a. The grain boundary is arranged parallel to the armchair direction. d is varied from 0 nm to 50 nm in two ranges: (i) 1 nm increments when d is close to the indenter tip to resolve failure loads influenced by contact between the tip and the grain boundary, and (ii) 5 nm increments when d is further away to identify the transition in failure mechanism from one of grain boundary rupture to one of structural instability.

The indenter tip is positioned immediately above the center of the membrane and is modeled as a rigid sphere of radius, $r_{tip} = 16.5$ nm, corresponding to the radius of the indenter tip used in experiments (Lee et al., 2008). The fracture load experimentally depends on r_{tip}, but for simplicity we do not vary r_{tip} in these simulations because we are focused on identifying the general failure characteristics of polycrystalline graphene.

The suspended membrane is meshed with bilinear quadrilateral membrane elements with an element edge length ranging from 20 nm far away from the grain boundary to 1 nm at the grain boundary and the contact zone beneath the indenter tip. Therefore, the length of the cohesive zone elements is $l^o = 1$ nm. The membrane elements along the grain boundary, adjacent to the cohesive elements, are constructed to be square to minimize mesh dependencies.

The suspended membrane is subject to a radial pre-stress of 0.335 N/m at the periphery prior to indentation to replicate the conditions measured in experiments (Lee et al., 2008). Subsequently, the membrane periphery is subject to a zero displacement boundary condition during the indentation. The bottom and top surfaces of the membrane, excluding the top surface area in contact with the indenter tip, are traction-free. The contact area is subject to a displacement boundary condition that depends on the displacement control of the indenter into the center of the top membrane surface. The contact is modeled as frictionless. We specify a displacement rate of the indenter tip such that quasistatic conditions hold.

The mechanical response of each grain is modeled with the experimentally-validated 5^{th}-order nonlinear anisotropic elastic constitutive relation described previously (Wei et al., 2009; Wei and Kysar, 2012). The grain boundary is modeled with the CZM

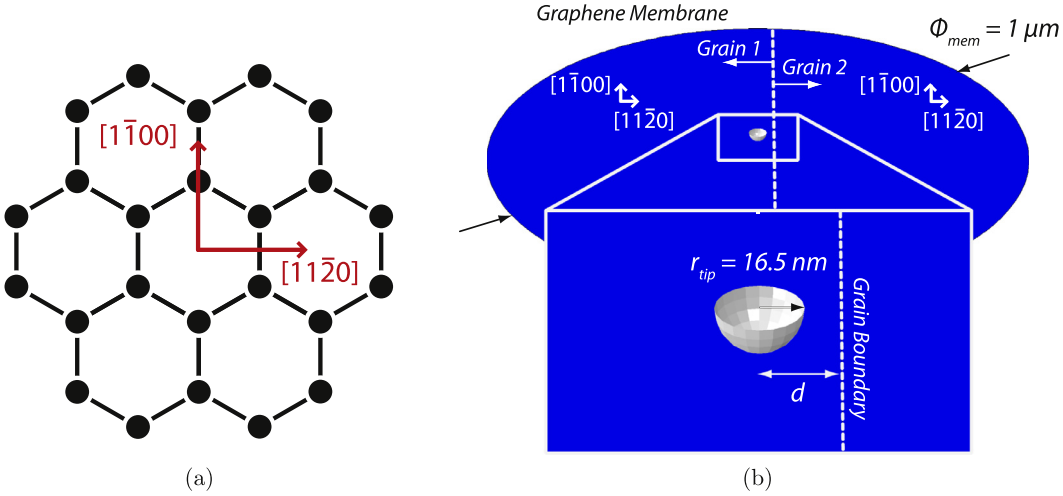

Fig. 8. (a) The crystal structure of a single graphene grain with material orientation. The black dots represent the carbon atoms and the straight black lines represent the covalent bonds between atoms. (b) A perspective view of the problem domain of a suspended circular two-grain graphene membrane with a single straight grain boundary subject to nanoindentation. The bottom center of the figure provides a magnified view of the center of the membrane.

proposed in Section 3.3 using the traction vs. separation relationship and material properties described in Section 3.1. These properties are implemented in ABAQUS/Standard as a User Material (UMAT) and a User Element (UEL), respectfully (Hibbitt et al., 2001).

There are two additional numerical controls that we specify for the simulation. As justified in Section 3.3, a linear MPC is used along the grain boundary to ensure the cohesive zone nodes are appropriately constrained. Additionally, ABAQUS/Standard contact controls are utilized to model the interaction between the indenter tip and the center of the suspended membrane with a state-based tracking algorithm for finite-sliding (Hibbitt et al., 2001). We apply displacement control to the indenter tip perpendicular into the center of the membrane at sufficiently small increments such that convergence is achieved. The solver is monitored until softening occurs, thus indicating that failure has occurred either due to structural instability (cf. Wei and Kysar, 2012) within a grain or rupture within the grain boundary. We account for finite deformation kinematics in the simulations.

5. Results and discussion

The onset and mode of failure is identified for each d and the corresponding critical fracture load, F_c, (the reaction force on the indenter tip at fracture) is recorded. In Fig. 9, we plot d vs. F_c to visualize the transition in failure modes and gain insight into factors that may influence the probability of failure. To ensure that our numerical implementation is self-consistent, we verified that the normal traction within the grain boundary at incipient failure is equal to the maximum stress of the traction vs. separation relationship.

There are three distinct regions to consider in Fig. 9 that we label as regions I, II, and III. In region I, the grain boundary is in contact with the indenter tip at the time of failure; the relationship between d and F_c is nonlinear and failure occurs within the grain boundary. As d increases into region II, the relationship between d and F_c becomes linear, but failure still occurs within the grain boundary. The transition from region II to III marks the critical distance, d_c, where the failure mechanism shifts from grain boundary failure to one of structural instability within the grain. In region III, the value of F_c plateaus and failure occurs at a constant maximum fracture load independent of d.

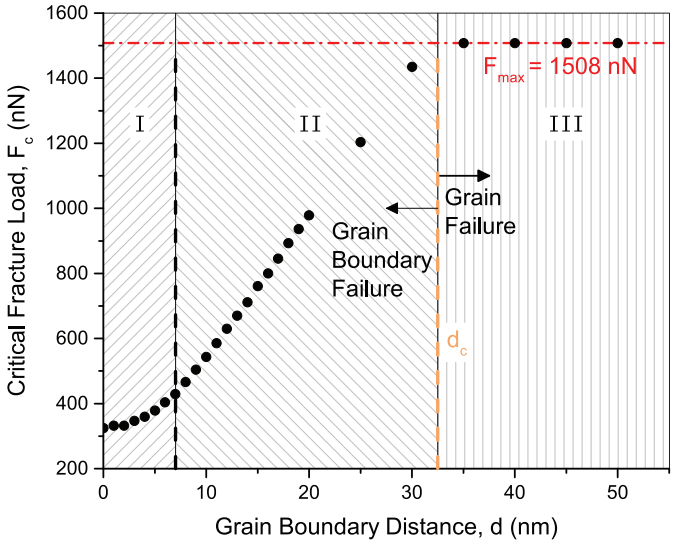

Fig. 9. Failure analysis for a suspended circular graphene membrane subject to a 16.5 nm radius indenter tip with a single straight grain boundary at varying distances, d, from the indentation point. The force beneath the indenter tip at the moment of failure, F_c, is plotted as function of grain boundary distance to the indenter tip, d.

The transition in failure mechanism between regions II and III that occurs at about 30 nm $< d_c <$ 35 nm is for the specified indenter tip radius and CZM parameters. As depicted in Fig. 9, for $d < d_c$, the grain boundary traction reaches its maximum strength prior to the point where graphene reaches its intrinsic strength. The onset of failure within the grain boundary is identified by the cohesive zone element that first reaches its maximum stress, σ_m, as defined by Eq. (3) and shown in Fig. 1. This point represents the moment before void nucleation within the grain boundary. Otherwise, for $d > d_c$, the material within the graphene grain reaches its peak strength and failure occurs due to a structural instability. The critical force for failure becomes constant because with increasing d the tractions in the grain boundary will only decrease and the grain will always rupture at the same fracture load.

Let us examine each of the three regions of Fig. 9 in more depth and consider the dependent parameters that influence the critical fracture load. Understanding these features is crucial for be-

ginning to deconstruct the probability of failure of polycrystalline graphene.

In region I, the relationship between d and F_c is nonlinear for $d \lesssim r_{tip}/2$. This response is likely due to contact effects between the indenter tip and the grain boundary at the time of failure. Consider the radius of contact between the indenter tip and the suspended membrane. The critical indentation depth, δ_c, of pristine graphene at rupture for an indenter radius of $r_{tip} = 16.5$ nm and a membrane diameter of 1 μm is $\delta_c = 104$ nm. With the introduction of a grain boundary in close proximity to the indenter tip, the indentation depth is less due to activation of the grain boundary defect ($\delta_c < 70$ nm). Therefore, only a fraction of the tip radius is in contact with the membrane upon failure. The distance beyond which the grain boundary is no longer in contact with the indenter tip at failure is determined to be $d = 8 \pm 1$ nm. Note that this value is only slightly lower than $r_{tip}/2$. It is reasonable to hypothesize that the nonlinearity in region I depends on the contact area between the indenter and the grain boundary and, hence, is a function of r_{tip}, ϕ_{mem}, and δ_c. In turn, δ_c is dependent on the properties of the grain boundary and grain.

Additionally, nanoindentation experiments on single crystal graphene have demonstrated that a larger indenter radius leads to a larger F_c, and therefore an increase in δ_c (Lee et al., 2008). Thus, a larger radius tip would result in an increased contact area upon failure. Hence, it is reasonable to suspect that the transition distance from region I to II would also increase with larger r_{tip} under constant material properties.

In region II, there is clearly a linear relationship between d and F_c. The grain boundary is at a sufficient distance from the indenter tip in that it is unaware of the tip's finite curvature and can be treated as a point load. Therefore, it is reasonable to expect F_c to be independent of r_{tip}. This hypothesis is supported by considering stress as a function of radial position upon failure of pristine graphene. Wei and Kysar (2012) showed that for a similar domain and boundary conditions, but in the absence of a grain boundary, there is a fairly linear relationship between stress and radial position for distances between 10 nm and 30 nm. It is reasonable to suspect that this linear relationship would translate to a linear relationship between F_c (i.e. the grain boundary reaching σ_m) and d within region II.

The behavior in region III becomes synonymous to the failure of a single crystal graphene membrane. The critical failure load becomes constant at $F_c = 1508$ nN for $d_c < d$ where failure occurs within the grain due to a structural instability. The membrane failure is essentially unaware of the presence of the grain boundary. Therefore, F_c becomes independent of d in this region. As a result, the transition between failure mechanisms occurs abruptly with increasing d. Again, we know from experimental observations that F_c in region III is dependent on r_{tip} (Lee et al., 2008). While the breaking force will remain constant with increasing d, F_c will increase with r_{tip}, and vice versa. For a specified F_c, as r_{tip} increases, the contact area between the indenter and the membrane also increases. As a result, the force on the indenter is spread out over a larger area and this translates to a lower stress in the film (i.e. force/area). Therefore, a greater F_c is required to reach the critical breaking strength of the membrane to cause failure.

Fig. 10 shows the interplay of the Cauchy stress field with the grain boundary and the indenter tip for each of the three failure regions. The grain boundary in each frame is identified by the vertical black line. From left to right, each column represents the results at a particular grain boundary distance, $d = 0$ nm, $d = 20$ nm, and $d = 45$ nm, respectively. The top row of frames shows the Cauchy stress field at the onset of failure. In Fig. 10a and b, failure occurs within the grain boundary and in Fig. 10c, failure occurs within the grain. The bottom row of frames shows the qualitative development of the stress field a few time increments after failure initiation to demonstrate that failure does indeed occur on the grain boundary. Fig. 10a′ and b′ reveal stress concentrations at the crack tip as the crack propagates. In Fig. 10c′, the hexagonal symmetry of the graphene crystal lattice is evident due to the six-fold symmetry of the Cauchy stress immediately beneath the indenter tip.

Overall, it is reasonable to suspect these three failure regions to exist for any variation in the indenter radius, the material properties within each grain, or the cohesive zone properties defined along the grain boundary. The only changes we expect are shifts in the critical distances that separate regions and the values of the critical forces.

In order to gain further confidence in the implementation and operation of the membrane-based CZM, we allow some simulations to progress beyond the point of void nucleation and continue through crack propagation. It is important to note that dynamic effects are not yet taken into account in these simulations, so the stress contours past failure serve only as qualitative observations. In Fig. 11, we show the maximum in-plane Cauchy stress state evolution immediately beneath the indenter tip before, during, and after failure for $d = 0$ (i.e. grain boundary directly beneath the indenter tip). The grain boundary is shown as being vertical and centered in each frame. The material properties and orientation, the specimen configuration, and the mechanical loading are consistent with mirror symmetry about grain boundary so we expect the crack that develops along the grain boundary to be Mode I. Magnified views of Fig. 11a–d are provided in Fig. 11a′–d′ to show clearer details of the stress field.

Fig. 11a and a′ shows the stress state immediately before void nucleation. This frame reveals clear mirror symmetry about the grain boundary, as well as stress concentration since the membrane is near rupture. Fig. 11b and b′ identifies the onset of grain boundary failure as the indenter tip advances an additional increment into the membrane. At the very center of the frame, softening of the stress can be seen, indicating that some portions of the grain boundary have exceeded the critical displacement, δ_n, and a void has nucleated.

Fig. 11c and c′ reveals the initial stages of crack growth. The stress contours here provide a clear picture of the commonly known Griffith crack: a finite of length crack with two stress concentrated tips advancing vertically from the point of void nucleation. Finally, Fig. 11d–f shows select stages as the indenter tip continues to depress into the circular membrane. The cohesive zone (or grain boundary) clearly "unzips" (the crack tip advances) and the indenter tip can be seen protruding through the opening. As the interfacial separation increases to ten times the critical opening, δ_n, the interface becomes approximately traction-free (i.e. a free surface). This stable crack growth provides qualitative evidence that the CZM is properly implemented and numerically stable.

Our results show that failure is dominated by the details of the stress concentrations near the tip. In this region, the membrane is made taut due to the loading of the indenter tip. While this may increase the depth of indentation for a given force, it will not affect the details of the stress concentration. Therefore, we do not expect the presence of ripples or wrinkles in the film to affect the force at which failure occurs. An additional important observation from these simulations is that the failure analysis for graphene with this set of CZM parameters would not be significantly affected by graphene's material anisotropy if a different crystallographic orientation of the graphene were employed. The nanoindentation of a circular suspended membrane imposes an approximately equibiaxial stress state in the region below the indenter tip. Wei et al. (2009) showed that graphene's material response does not become anisotropic until ~15% strain. For these CZM parameters, the grain boundary ruptures at ~7% strain, well below

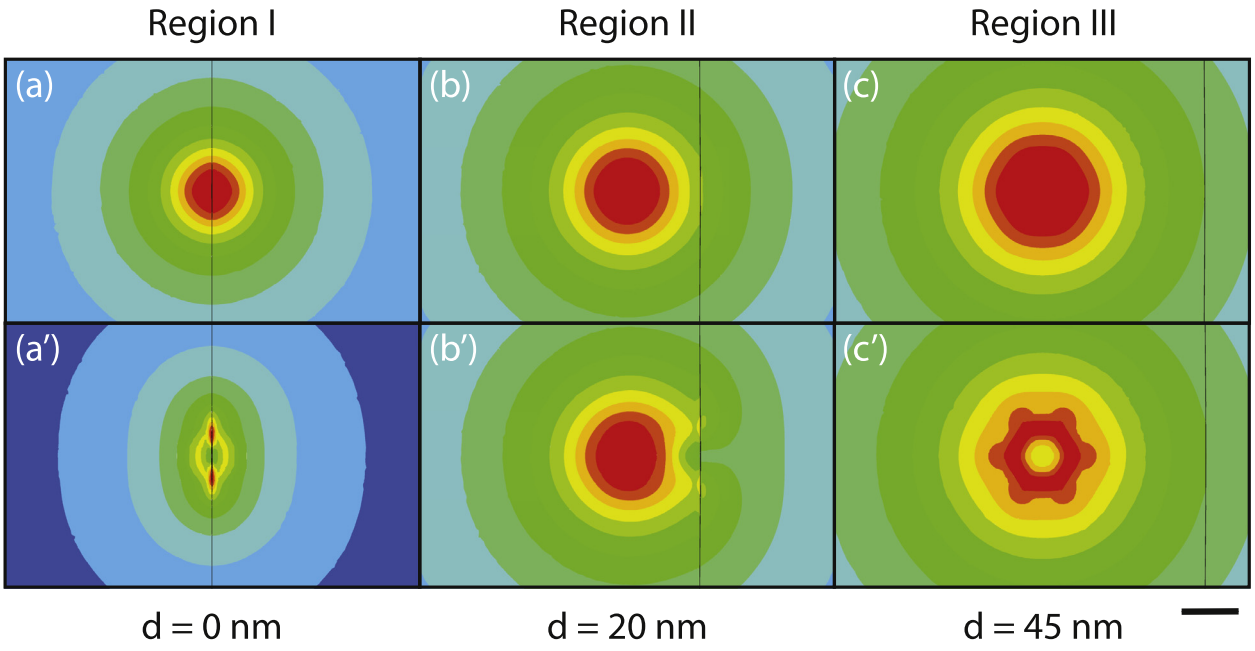

Fig. 10. Maximum in-plane Cauchy stress field for selected grain boundary distances within each failure region. The grain boundary within each frame is indicated by the vertical black line. (a)–(c) The onset of failure for grain boundary distances of 0 nm, 20 nm, and 45 nm, respectively. (a′)–(c′) A few increments after the onset of failure at the corresponding grain boundary distances (scale ∼20 nm).

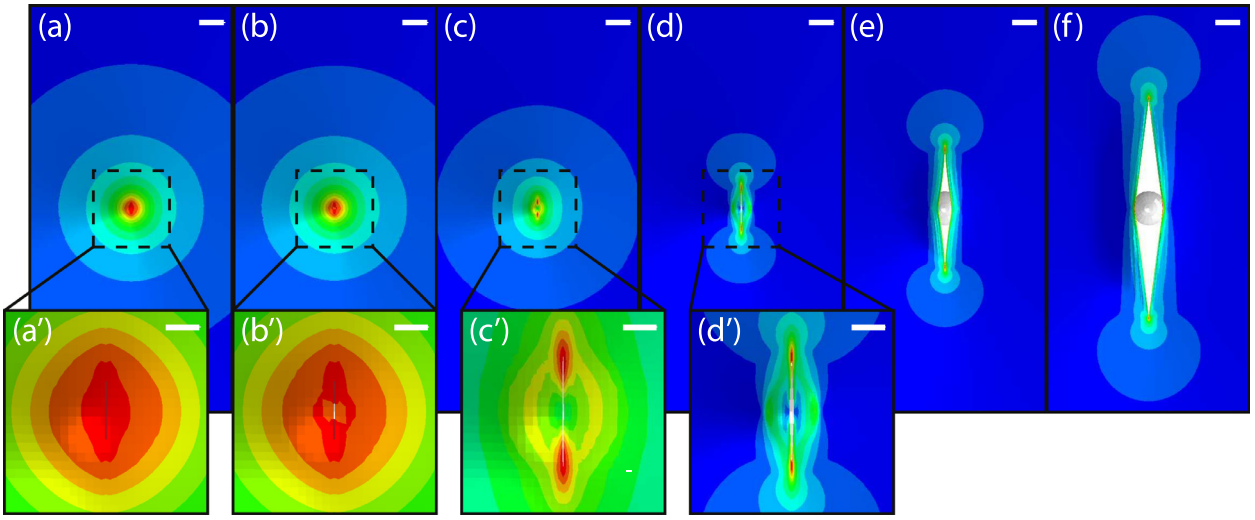

Fig. 11. Maximum in-plane Cauchy stress for a grain boundary immediately beneath the indenter tip. (a)–(f) Characteristic stages of a grain boundary at the moments before, during, and after failure with a 16.5nm radius indenter tip (scale ∼10 nm). (a′)–(d′) Select magnified views for better resolution (scale ∼5 nm).

the threshold at which graphene begins to exhibit anisotropic behavior. Hence, these results would hold for any variety of aligned or mismatched grain orientations and the threshold distance, d_c, that defines the transition between failure modes can be considered the threshold radius, instead. However, if the strength of the grain boundary is very close to that of the pristine material, then mechanical anisotropy may affect the results, although we expect this to be a second-order effect.

6. Conclusions

We have introduced the formulation of a Cohesive Zone Model (CZM) for a membrane element. The details of the kinematics of the CZM were proposed for determining the separation across the interface. To account for the under-constrained nature of a two-dimensional element spanning three-dimensional space, we applied numerical controls through a Multiple Point Constraint (MPC). The MPC requires the cohesive zone element together with its two adjacent membrane elements to maintain bilinearity as a whole.

The traction vs. separation relationship that governs the CZM is based on MD simulations of experimentally observed defect structures in graphene grain boundaries. As discussed by Guin et al. (2016), a typical high angle grain boundary consists of a continuous defect structure. A low angle grain boundary contains periodic defects separated by regions of perfect lattice (i.e. not a continuous defect structure). Consequently, our model is not expected to model low angle grain boundaries adequately.

We implemented the membrane-based CZM within the context of a suspended circular graphene bicrystal subject to nanoindentation. ABAQUS/Standard FEM software was utilized to model the nanoindentation experiment. The model identifies two potential

failure modes: (i) grain boundary rupture due to void nucleation within the CZM, and (ii) grain failure due to a structural instability. We ran simulations to failure with incremental grain boundary distances from immediately beneath the indenter tip to a distance such that a transition in failure mechanism was identified.

As a result, we presented the failure analysis plot in Fig. 9 that shows the critical fracture load, F_c, as a function of grain boundary distance, d. There are three distinct regions where we consider the factors that influence failure: I, II, and III. The division between regions II and III identifies the critical threshold distance, d_c, between failure modes. For $d < d_c$, failure occurs within the grain boundary, while for $d > d_c$ failure occurs within the grain. Region I shows clear nonlinearity that we attribute to contact with the indenter tip upon grain boundary rupture and therefore we expect dependence on r_{tip}. On the contrary, we suspect that the linear slope in region II is independent of r_{tip} because the grain boundary is sufficiently far that it sees the indenter tip as a point load. In region III, F_c becomes constant due to a transition of failure mechanisms. Failure occurs within the grain due to a structural instability and becomes independent of d.

The formulation of this membrane-based CZM allows further studies of more complicated and realistic polycrystalline graphene domains. In future studies, we will examine the effect of r_{tip} on the probability of failure and we will consider randomly generated grain structures to more accurately capture the experimentally observed structures. Additionally, these results establish the foundation to systematically vary the cohesive zone parameters to investigate their effects on the transitions between failure regions. A future direction of this research results will be to use this model through an inverse analysis in order to analyze experiments of polycrystalline graphene, such as the ones performed by Lee et al. (2013), to determine the grain boundary strength. Ultimately, this model provides a means to study the probability of failure of polycrystalline CVD-grown graphene.

Acknowledgments

This work was supported by the National Science Foundation under awards NSF-1437450 and NSF-1363093. The authors are thankful for fruitful conversations with Professor Haim Waisman from The Department of Civil Engineering and Engineering Mechanics at Columbia University.

References

Alian, A., Meguid, S., 2017. Hybrid molecular dynamics-finite element simulations of the elastic behavior of polycrystalline graphene. Int. J. Mech. Mater. Des. doi:10.1007/s10999-017-9389-y.

Barenblatt, G.I., 1959. The formation of equilibrium cracks during brittle fracture. General ideas and hypotheses. axially-symmetric cracks. J. Appl. Math. Mech. 23 (3), 622–636.

Becker, R., 1988. Interface constitutive relations for use with the finite element code abaqus. Memorandum KZ-002, 15212. Fabricating Technology-B Group, Alcoa, Pittsburgh, Pennsylvania.

Becton, M., Zeng, X., Wang, X., 2015. Computational study on the effects of annealing on the mechanical properties of polycrystalline graphene. Carbon 86, 338–349.

Cao, A., Yuan, Y., 2012. Atomistic study on the strength of symmetric tilt grain boundaries in graphene. Appl. Phys. Lett. 100 (21), 211912.

Chen, M., Quek, S., Sha, Z., Chiu, C., Pei, Q., Zhang, Y., 2015. Effects of grain size, temperature and strain rate on the mechanical properties of polycrystalline graphene–a molecular dynamics study. Carbon 85, 135–146.

Dugdale, D.S., 1960. Yielding of steel sheets containing slits. J. Mech. Phys. Solids 8 (2), 100–104.

Grantab, R., Shenoy, V.B., Ruoff, R.S., 2010. Anomalous strength characteristics of tilt grain boundaries in graphene. Science 330 (6006), 946–948.

Griffith, A.A., 1921. The phenomena of rupture and flow in solids. Philos. Trans. R. Soc. Lond. Ser. A Contain. Pap. Math. Phys. Character 221, 163–198.

Guin, L., Raphanel, J.L., Kysar, J.W., 2016. Atomistically derived cohesive zone model of intergranular fracture in polycrystalline graphene. J. Appl. Phys. 119 (24), 245107.

Han, J., Ryu, S., Sohn, D., Im, S., 2014. Mechanical strength characteristics of asymmetric tilt grain boundaries in graphene. Carbon 68, 250–257.

Hao, F., Fang, D., 2012. Mechanical deformation and fracture mode of polycrystalline graphene: atomistic simulations. Phys. Lett. A 376 (24–25), 1942–1947.

Hibbitt, Karlsson, Sorensen, 2001. ABAQUS/Standard User's Manual, 1. Hibbitt, Karlsson & Sorensen.

Hillerborg, A., Modéer, M., Petersson, P.-E., 1976. Analysis of crack formation and crack growth in concrete by means of fracture mechanics and finite elements. Cem. Concr. Res. 6 (6), 773–781.

Huang, P.Y., Ruiz-Vargas, C.S., van der Zande, A.M., Whitney, W.S., Levendorf, M.P., Kevek, J.W., Garg, S., Alden, J.S., Hustedt, C.J., Zhu, Y., Park, J., McEuen, P.L., Muller, D.A., 2011. Grains and grain boundaries in single-layer graphene atomic patchwork quilts. Nature 469 (7330), 389–392.

Jhon, Y.I., Chung, P.S., Smith, R., Min, K.S., Yeom, G.Y., Jhon, M.S., 2013. Grain boundaries orientation effects on tensile mechanics of polycrystalline graphene. RSC Adv. 3 (25), 9897–9903.

Jhon, Y.I., Zhu, S.-E., Ahn, J.-H., Jhon, M.S., 2012. The mechanical responses of tilted and non-tilted grain boundaries in graphene. Carbon 50 (10), 3708–3716.

Jung, G., Qin, Z., Buehler, M.J., 2015. Molecular mechanics of polycrystalline graphene with enhanced fracture toughness. Extreme Mech. Lett. 2, 52–59.

Khare, R., Mielke, S.L., Paci, J.T., Zhang, S., Ballarini, R., Schatz, G.C., Belytschko, T., 2007. Coupled quantum mechanical/molecular mechanical modeling of the fracture of defective carbon nanotubes and graphene sheets. Phys. Rev. B 75 (7), 075412.

Kim, K.S., Zhao, Y., Jang, H., Lee, S.Y., Kim, J.M., Kim, K.S., Ahn, J.-H., Kim, P., Choi, J.-Y., Hong, B.H., 2009. Large-scale pattern growth of graphene films for stretchable transparent electrodes. Nature 457 (7230), 706.

Kotakoski, J., Meyer, J.C., 2012. Mechanical properties of polycrystalline graphene based on a realistic atomistic model. Phys. Rev. B 85 (19), 195447.

Larsson, R., Samadikhah, K., 2011. Atomistic continuum modeling of graphene membranes. Comput. Mater. Sci 50 (5), 1744–1753.

Lee, C., Wei, X., Kysar, J.W., Hone, J., 2008. Measurement of the elastic properties and intrinsic strength of monolayer graphene. Science 321 (5887), 385–388.

Lee, G.-H., Cooper, R.C., An, S.J., Lee, S., van der Zande, A., Petrone, N., Hammerberg, A.G., Lee, C., Crawford, B., Oliver, W., et al., 2013. High-strength chemical-vapor–deposited graphene and grain boundaries. Science 340 (6136), 1073–1076.

Li, X., Cai, W., An, J., Kim, S., Nah, J., Yang, D., Piner, R., Velamakanni, A., Jung, I., Tutuc, E., et al., 2009a. Large-area synthesis of high-quality and uniform graphene films on copper foils. Science 324 (5932), 1312–1314.

Li, X., Cai, W., Colombo, L., Ruoff, R.S., 2009b. Evolution of graphene growth on ni and cu by carbon isotope labeling. Nano Lett. 9 (12), 4268–4272.

Liu, T.-H., Gajewski, G., Pao, C.-W., Chang, C.-C., 2011. Structure, energy, and structural transformations of graphene grain boundaries from atomistic simulations. Carbon 49 (7), 2306–2317.

Liu, T.-H., Pao, C.-W., Chang, C.-C., 2012. Effects of dislocation densities and distributions on graphene grain boundary failure strengths from atomistic simulations. Carbon 50 (10), 3465–3472.

Liu, Y., Yakobson, B.I., 2010. Cones, pringles, and grain boundary landscapes in graphene topology. Nano Lett. 10 (6), 2178–2183.

Malola, S., Häkkinen, H., Koskinen, P., 2010. Structural, chemical, and dynamical trends in graphene grain boundaries. Phys. Rev. B 81 (16), 165447.

Mortazavi, B., Cuniberti, G., 2014. Atomistic modeling of mechanical properties of polycrystalline graphene. Nanotechnology 25 (21), 215704.

Needleman, A., 1987. A continuum model for void nucleation by inclusion debonding. J. Appl. Mech. 54 (3), 525–531.

Novoselov, K.S., Geim, A.K., Morozov, S.V., Jiang, D., Zhang, Y., Dubonos, S.V., Grigorieva, I.V., Firsov, A.A., 2004. Electric field effect in atomically thin carbon films. Science 306 (5696), 666–669.

Rasool, H.I., Ophus, C., Zhang, Z., Crommie, M.F., Yakobson, B.I., Zettl, A., 2014. Conserved atomic bonding sequences and strain organization of graphene grain boundaries. Nano Lett. 14 (12), 7057–7063.

Rose, J.H., Ferrante, J., Smith, J.R., 1981. Universal binding energy curves for metals and bimetallic interfaces. Phys. Rev. Lett. 47 (9), 675.

Sha, Z., Quek, S., Pei, Q., Liu, Z., Wang, T., Shenoy, V., Zhang, Y., 2014a. Inverse pseudo Hall–Petch relation in polycrystalline graphene. Sci. Rep. 4, 5991.

Sha, Z., Wan, Q., Pei, Q., Quek, S., Liu, Z., Zhang, Y., Shenoy, V., 2014b. On the failure load and mechanism of polycrystalline graphene by nanoindentation. Sci. Rep. 4, 7437.

Shekhawat, A., Ritchie, R.O., 2016. Toughness and strength of nanocrystalline graphene. Nat. Commun. 7, 10546.

Song, Z., Artyukhov, V.I., Yakobson, B.I., Xu, Z., 2013. Pseudo Hall–Petch strength reduction in polycrystalline graphene. Nano Lett. 13 (4), 1829–1833.

Taylor, R., Oñate, E., Ubach, P.-A., 2005. Computational methods in applied sciences. In: Oñate, Eugenio (Ed.), Textile Composites and Inflatable Structures, volume 3, chapter Finite element analysis of membrane structures. Springer, Dordrecht, pp. 47–68.

Wang, X., Guo, X., 2013. Quasi-continuum model for the finite deformation of single-layer graphene sheets based on the temperature-related higher order cauchy-born rule. J. Comput. Theor. Nanosci. 10 (1), 154–164.

Wei, X., Fragneaud, B., Marianetti, C.A., Kysar, J.W., 2009. Nonlinear elastic behavior of graphene: ab initio calculations to continuum description. Phys. Rev. B 80 (20), 205407.

Wei, X., Kysar, J.W., 2012. Experimental validation of multiscale modeling of indentation of suspended circular graphene membranes. Int. J. Solids Struct. 49 (22), 3201–3209.
Wei, Y., Wu, J., Yin, H., Shi, X., Yang, R., Dresselhaus, M., 2012. The nature of strength enhancement and weakening by pentagon–heptagon defects in graphene. Nat. Mater. 11 (9), 759.
Wu, J., Wei, Y., 2013. Grain misorientation and grain-boundary rotation dependent mechanical properties in polycrystalline graphene. J. Mech. Phys. Solids 61 (6), 1421–1432.
Xu, X.-P., Needleman, A., 1993. Void nucleation by inclusion debonding in a crystal matrix. Model. Simul. Mater. Sci. Eng. 1 (2), 111.
Yang, Z., Huang, Y., Ma, F., Sun, Y., Xu, K., Chu, P.K., 2015. Size-dependent deformation behavior of nanocrystalline graphene sheets. Mater. Sci. Eng. B 198, 95–101.
Yazyev, O.V., Louie, S.G., 2010. Topological defects in graphene: dislocations and grain boundaries. Phys. Rev. B 81 (19), 195420.
Yi, L., Yin, Z., Zhang, Y., Chang, T., 2013. A theoretical evaluation of the temperature and strain-rate dependent fracture strength of tilt grain boundaries in graphene. Carbon 51, 373–380.
Zhang, H., Duan, Z., Zhang, X., Liu, C., Zhang, J., Zhao, J., 2013. Strength and fracture behavior of graphene grain boundaries: effects of temperature, inflection, and symmetry from molecular dynamics. Phys. Chem. Chem. Phys. 15 (28), 11794–11799.
Zhang, J., Zhao, J., Lu, J., 2012. Intrinsic strength and failure behaviors of graphene grain boundaries. ACS Nano 6 (3), 2704–2711.
Zhang, T., Li, X., Gao, H., 2015a. Fracture of graphene: a review. Int. J. Fract. 196 (1–2), 1–31.
Zhang, Z., Yang, Y., Xu, F., Wang, L., Yakobson, B.I., 2015b. Unraveling the sinuous grain boundaries in graphene. Adv. Funct. Mater. 25 (3), 367–373.